

Full length article

Linking microstructure and local mechanical properties in SiC-SiC fiber composite using micromechanical testing

Yevhen Zayachuk^{a,*}, Phani Karamched^a, Christian Deck^b, Peter Hosemann^{c,d}, David E.J. Armstrong^a^a University of Oxford, Department of Materials, Parks Road, Oxford, OX1 3PH, UK^b General Atomics, P.O. Box 85608, San Diego, CA, 92186-5608, USA^c Department of Nuclear Engineering, University of California, Etcheverry Hall, 2521 Hearst Ave, Berkeley, CA, 94709, USA^d Lawrence Berkeley National Laboratory, Berkeley, CA, 94720, USA

ARTICLE INFO

Article history:

Received 11 September 2018

Received in revised form

1 February 2019

Accepted 2 February 2019

Available online 6 February 2019

Keywords:

Silicon carbide

Ceramic matrix composites

Micromechanics

Transmission electron microscopy

ABSTRACT

Local mechanical properties of SiC-SiC fiber-reinforced composite – matrix, fiber and interphases – were evaluated using nanoindentation and microcantilever fracture testing. The fracture toughness was found to be $\sim 4.25 \text{ MPa}\cdot\text{m}^{1/2}$ in the matrix, $\sim 2 \text{ MPa}\cdot\text{m}^{1/2}$ in the fibers and $\sim 0.8 \text{ MPa}\cdot\text{m}^{1/2}$ at the interphases. Nanoindentation hardness was found to vary from $\sim 17 \text{ GPa}$ in the center of the fibers to $\sim 40 \text{ GPa}$ in the matrix. Values obtained with micromechanical testing were found to be in good agreement with the available data on bulk mechanical properties. The mechanical property variations in the different components of the composite can be explained by the variations in the microstructure. The matrix has complex hierarchical microstructure with elongated grains, often featuring twinning, growing radially from the fibers in predominantly $\langle 111 \rangle$ direction and forming sets of concentric rings around them. The fibers contain equiaxed grains with carbon precipitates at the grain boundaries. It was found that in the matrix fracture is transgranular, while in the fibers it can be both trans- and intergranular; at the interphases the fracture occurs at the carbon-fiber boundary. The differences in mechanical properties between the matrix and the fibers are attributed to the presence of carbon inclusions in the fibers, which reduce both hardness and fracture toughness.

© 2019 Acta Materialia Inc. Published by Elsevier Ltd. This is an open access article under the CC BY license (<http://creativecommons.org/licenses/by/4.0/>).

1. Introduction

Silicon carbide (SiC) has a number of beneficial properties making it an attractive option for applications where a structural material able to withstand extreme, particularly high-temperature, environments is required. These include high temperature strength and creep resistance [1], and oxidation resistance [2]. Its practical use, however, is hindered by its inherent brittleness [3]. In order to overcome the inherently low toughness of SiC, it is suggested to be used in the form of a continuous SiC fiber-reinforced SiC matrix (SiC-SiC) composite [4].

In particular, SiC-SiC composites are used in aero-engines, which also benefit from the light weight of SiC [5]. Prominent application is the high-pressure turbine shrouds of CFM LEAP engines [6,7]; the use of SiC is also expected in the inner and outer

combustor liners and high-pressure turbine nozzles in the GE9X engines, and other components [8].

Also there is a considerable interest to deploy SiC-SiC composites in nuclear technology, thanks to abovementioned high-temperature properties but also its radiation tolerance [9,10]. It is suggested to be used in accident tolerant fuel (ATF) – an alternative fuel form which would mitigate the hydrogen production during a severe accident and minimise the danger of the subsequent explosions (such as the ones that happened in Fukushima accident) [11] – where SiC would serve as a fuel cladding material [12,13].

Fiber composite is formed by growing the SiC matrix onto a woven or braided reinforcing SiC fiber structure. Several methods of manufacturing the matrix of this kind have been proposed. These include melt infiltration [14,15], polymer infiltration and pyrolysis (PIP) [16], transient eutectic phase (TEP) [17] and chemical vapour infiltration (CVI) [18]. Among these, CVI has an advantage of being able to produce very high purity β -phase SiC which has good radiation resistance [19] and is therefore advantageous for use in

* Corresponding author.

E-mail address: yevhen.zayachuk@materials.ox.ac.uk (Y. Zayachuk).

nuclear environments; the drawbacks of it are that CVI process is slow and might require several weeks of infiltration time [20], as well as leaves behind extensive porosity that is not reproducible from run to run, and leads to poor reproducibility in mechanical properties. In this method, a gaseous SiC precursor, such as methyltrichlorosilane (CH_3SiCl_3) mixed with hydrogen, is introduced into a high temperature chamber where the pre-fabricated fiber structure is located, chemically reacts with hydrogen and decomposes forming a silicon carbide matrix within and around the fiber reinforcement, forming the composite [21].

The presence of the reinforcement leads to a pseudo ductility during deformation due to crack deflections and crack bridging [22,23]. As a consequence, the overall properties of a composite are determined by the properties of the constituents and interaction between them [24]. Therefore, in order to be able to construct a microstructurally informed model able to reliably predict the components' behaviour it is necessary to thoroughly characterize the mechanical behaviour of the individual constituents of the material [25]. This is difficult as the typical length scales range from 10's of nanometers for interlayers between fibre and matrix to $\sim 10\ \mu\text{m}$ for fibre diameters. Micro-mechanical testing methods, including micro-bending and nanoindentation experiments are well placed to do this but need validating against bulk data.

This contribution presents the results and interpretation of the local property measurements of a SiC-SiC composite. The microstructure was investigated using various electron microscopy tools, with the emphasis on revealing the property and microstructural differences between fiber and matrix materials and on linking these to mechanical behaviour. Nanoindentation was used for the comparison of mechanical properties of matrix and fiber materials. The difference between them, as well as the properties of the fiber-matrix interphases, was further studied by the fracture tests using microcantilevers manufactured by focused ion beam milling within fiber, matrix and at interphases; in these tests the values of fracture stress and strain, as well as fracture toughness, were determined. The results of the micromechanical measurements were validated by comparison with bulk measurements reported in the literature and rationalized by comparing them with the microstructure of the corresponding constituents of the composite.

2. Experimental

The material used in this study was manufactured by General Atomics (San Diego, US). Commercially available Tyranno SA3 fibers (Ube Industries Ltd [26,27]) were used for the in-house manufacturing of interwoven reinforcement structure with plain weave architecture. These fibers were coated by $\sim 100\ \text{nm}$ thick layer of pyrolytic carbon (PyC). Subsequently, the matrix was grown onto the coated fibres using the CVI method (as described in Ref. [21]). For this investigation, samples were cut from 10 by 10 mm, $\sim 1\ \text{mm}$ thick sheets using a Capco diamond saw, resulting in 10 mm long bars with the cross section of 1 mm by $\sim 700\ \mu\text{m}$. These samples were ground mechanically using SiC grinding discs, followed by the fine polishing using diamond suspension of 3 and $1\ \mu\text{m}$ size, revealing the fibers running through the matrix, parallel and perpendicular to the examined surface.

The microstructure was characterized by secondary electron microscopy (SEM), scanning transmission electron microscopy (STEM), energy-dispersive X-ray spectroscopy (EDX), electron backscatter diffraction (EBSD), and transmission Kikuchi diffraction (TKD), assisted by focused ion beam (FIB). STEM and TKD samples of $\sim 100\ \text{nm}$ thickness were made using FIB lift-out [28] in the ZEISS Auriga dual-beam FEG SEM-FIB workstation equipped with

Kleindiek MM3A micromanipulator; the same workstation was also used for SEM imaging. STEM imaging was performed using a JEOL JEM-2100 TEM with energy-dispersive X-ray spectroscopy (EDX) capability used for elemental analysis. EBSD was performed using a JEOL-6500 FEG-SEM. In order to remove the surface damage caused by mechanical polishing and improve the backscatter electron signal quality, ion polishing was implemented [29], using a Gatan PECS-II Ar ion polishing setup. TKD was performed using on-axis detector in Zeiss Merlin FEG-SEM equipped with Quantax EBSD detector with Optimus TKD detector head.

In order to characterise micromechanical properties over the large areas and in particular to compare the properties of the major composite's constituents – fibers and matrix – nanoindentation was used, performed with the Agilent XP nanoindenter in the continuous stiffness measurement (CSM) mode with 2 nm amplitude and 42 Hz frequency, using a Berkovich tip [30]. Hardness and elastic modulus were determined using the Oliver-Pharr method as a function of indentation depth. Calibration of the area function of the tip was performed on fused silica.

For assessment of the fracture properties of the fibers and matrix materials, as well as interphases, microcantilever fracture tests were used [31]. Triangular cantilevers were manufactured using FIB milling, following the procedure described in Ref. [32] leading to the geometry displayed in Fig. 1a). Typical dimensions of cantilevers used in this study were $\sim 8\ \mu\text{m}$ in length, $\sim 2\ \mu\text{m}$ in width, and $\sim 1.5\ \mu\text{m}$ in height. The fracture testing was performed using a Berkovich tip in an Agilent G200 nanoindenter equipped with a nano-positioning stage. The load-displacement curve is recorded and using simple beam theory, these were converted into stress-strain curves, which were used for determination of fracture stress and strain.

The notched cantilevers were used to measure fracture toughness, following the method described in Ref. [33]. In these cantilevers, which also had triangular cross-section, the straight notches were made by FIB milling at low current (10 pA) normally to the top surface and to the length of the cantilevers (Fig. 1d). The typical depth of these notches was $\sim 300\ \text{nm}$, and typical width $\sim 100\ \text{nm}$. The notches in these cantilevers were placed on the interphases of the fibers that are parallel to the surface of a sample, so that the interphase is following the length of a (straight) fiber, as in Fig. 1e.

3. Results and discussion

3.1. Microstructure

Fig. 2a presents a general view of the polished surface of the sample. The fiber bundles are clearly visible, both the ones perpendicular to the surface and those parallel to it. The presence of large pores between the bundles is evident. Fig. 2b presents a more detailed view of the vicinity of one of the fiber bundles. It emphasizes the lower-scale intra-bundle porosity with pores located between the individual fibers within the bundle. It is important to note that at larger magnification individual fibers can be easily resolved (Fig. 2c, denoted by arrows), which enables the precise aiming at the regions of interest (individual fibers, interphases or inter-fiber regions) for micromechanical testing and lifting out the TEM samples. Each fiber is so noticeable thanks to the presence of the dark thin “halos” surrounding each fiber, which are carbon interlayers. The distribution of porosity within the bundle is non-uniform. For the most part pores are concentrated close to the center of a bundle, where the areal concentration of the fibers is highest. Conversely, at the periphery of a bundle individual fibers are further apart, and each is surrounded by a monolithic block of matrix material with relatively few or no large pores, as shown in Fig. 2c.

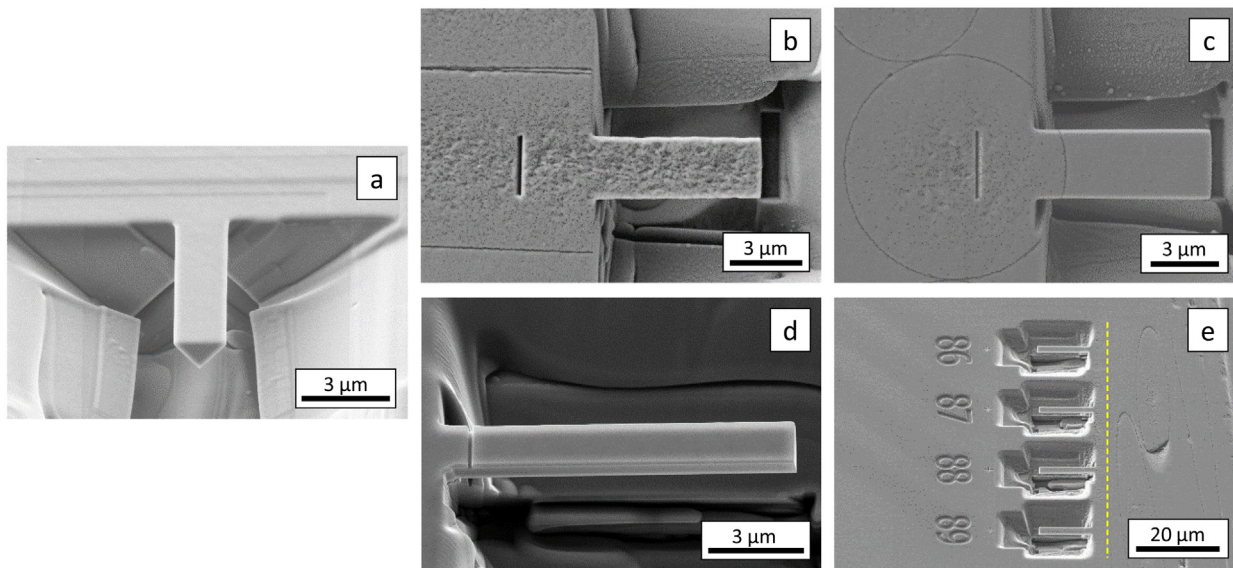


Fig. 1. Cantilevers located in the different components of the composite: (a) in the matrix, triangular cross-section is visible; (b) within the fiber; note the line near the base – this is a mark used for scanning and offset calculation; (c) at the interphase; (d) straight-notched cantilever in the matrix; (e) general geometry of the cantilevers at the interphase of a fiber parallel to the surface (fiber direction is denoted by dashed line).

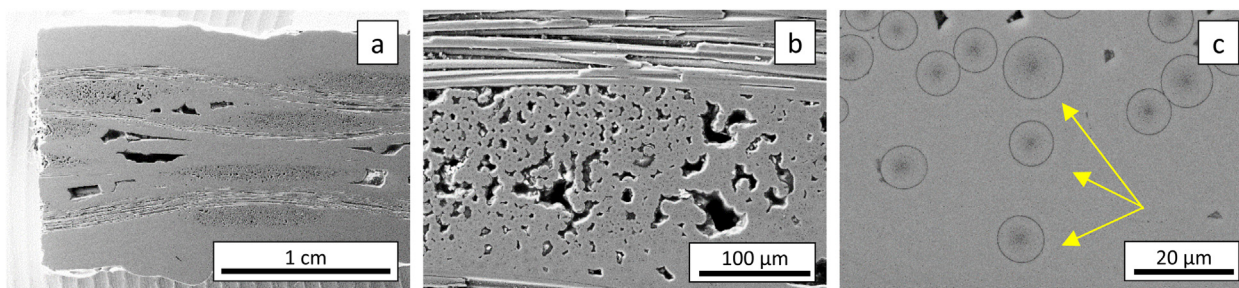


Fig. 2. SEM images of the polished surface of the composite: (a) general appearance, (b) close-up of the vicinity of a fiber bundle, (c) close-up with individual fibers, denoted by the arrows.

This difference in porosity within an individual fiber bundle is easy to understand, as during the growth of the matrix from the vapour phase the fibers serve as sites for crystallization. When there are multiple sites in the vicinity, as is the case in the centers of the bundles where concentration of fibers is highest, eventually the matrix layers growing from different fibers join together, not allowing further gas to penetrate deeper, resulting in multiple closed pores in the centers of the bundles. This doesn't happen at the periphery of a bundle, where the distances between the fibers are much larger and hence the layers of matrix can grow unimpeded.

The microstructure was investigated in greater detail using STEM and EBSD. Fig. 3a presents a general view of a typical area with several relatively close-by fibers (with separation of the order of $\sim 10\ \mu\text{m}$, typical for the periphery of the fibers) and surrounding matrix region. An inherent weakness of TEM, which only allows analysis of a small localized area (corresponding to a single lamella) at a time, making the investigation of the large areas difficult and time-consuming. At the same time, such an investigation is essential since microstructure is very non-uniform in such a composite. An alternative way of large-scale microstructure characterization is provided by image quality (IQ) mapping using EBSD ([34]), where each location is assigned a value reflecting the ability of an indexing software to detect Kikuchi bands, producing a

grayscale map ([35]). Fig. 3b presents the IQ map of a typical area at the periphery of a fiber bundle, where fibers are relatively far apart and large regions of bulk matrix material are present.

It is evident that microstructure of the matrix is complex, being organized in several hierarchical levels. First of all, it consists of the grains elongated in the direction away from the fibers. Such directional growth is typical for SiC grown by CVI [36]. The close-up of these grains is shown in Fig. 3c. Their width is $\sim 100\text{--}200\ \text{nm}$, and their length is in the order of $\sim 2\text{--}5\ \mu\text{m}$. The matrix grains contain fine structure within them, consisting of series of parallel dark fringes, running approximately normally to the grain growth direction. Comparison with similar structures presented in the literature (e.g. Refs. [37,38]), indicates that these are likely stacking faults. In the regions of matrix in between fibers the growth of grains is constrained by the presence of other grains, originating at another fiber and growing in the opposite direction. At these interfaces porosity is found, running along the boundary between the domains, parallel to the direction of the fibers, as shown in Fig. 3d.

These grains are organized into ring-like structures. Notably, each fiber is surrounded by several nested rings (Fig. 3a and b). These are thought to originate from the discontinuities during the infiltration, with each ring corresponding to a consecutive stage of the matrix growth process. Finally, these rings form domains of

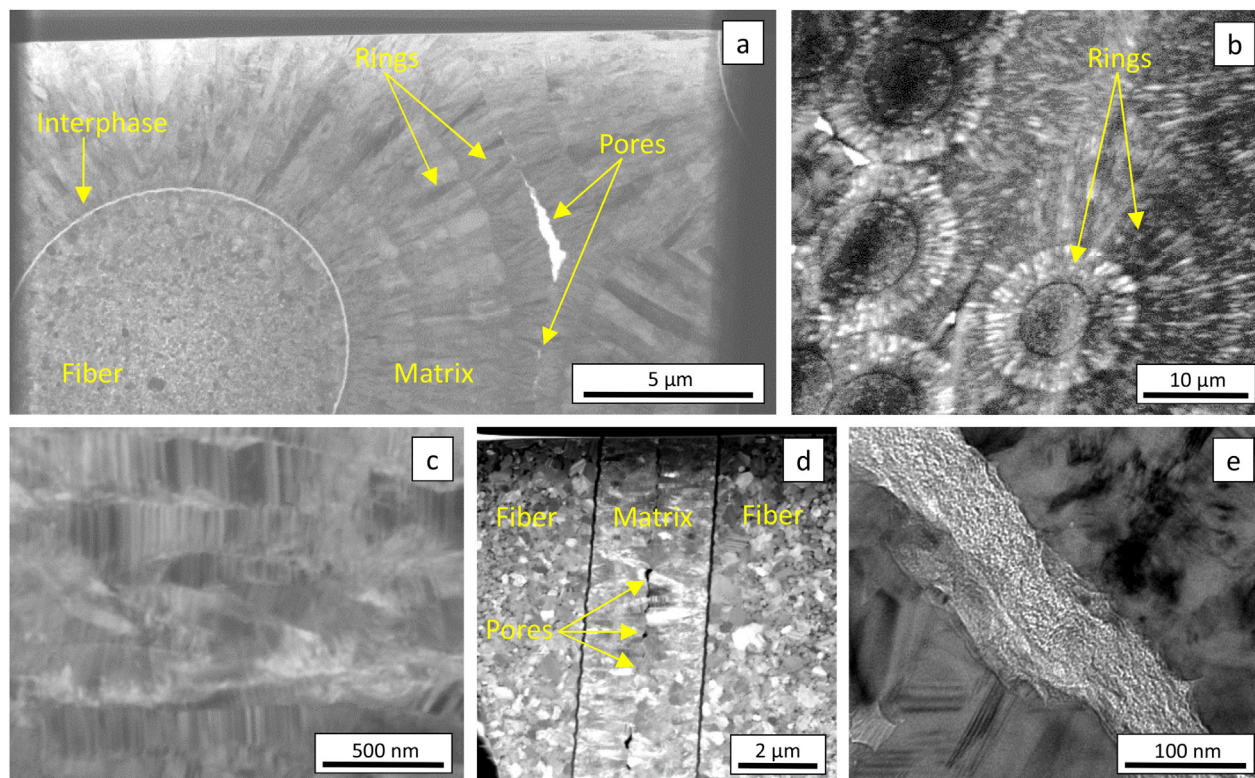


Fig. 3. (a) STEM image of a typical region containing fibers and surrounding matrix, arrows indicate submicron-sized pores; (b) Image quality map of a large area, including several fibers and a surrounding region of the matrix; (c) STEM image of the matrix material; (d) STEM image of the matrix ligament between two closely located fibers, arrows indicate submicron-sized pores; (e) TEM image of the interlayer.

matrix associated with each fiber. Observed multiple levels of microstructural organization give rise to multiple types of boundaries within the matrix. Elongated radial grains are separated by the regular grain boundaries. Nested concentric rings are separated by the inter-ring boundaries, and finally matrix domains are separated by the domain boundaries. And indeed these domain boundaries are the regions associated with the submicron-sized porosity observed in STEM images (Fig. 3b, d). The presence of these boundaries, together with the submicron-sized porosity, within the matrix indicates that the matrix itself is non-uniform, giving rise to the possibility that mechanical properties, and in particular fracture properties, are locally non-uniform as well. This has been investigated by micromechanical testing, as described in Section 3.3.

Fig. 3e shows the structure of a typical interlayer. It consists of a single layer of material with the thickness of ~100 nm and is amorphous.

Fig. 4a presents the close-up of the structure of the fiber material. It consists of essentially equiaxed grains, with typical grain size in the 50–200 nm range, comparable to the width of the elongated grains in the matrix. Microstructure is also radially non-uniform within the fiber – grain size is smallest in the center of a fiber (as denoted by a dashed line) and increases towards its periphery. It is interesting to note that the grain boundaries are often associated with inclusions (Fig. 4b, dark in this imaging mode, indicated by arrows). Fig. 4c shows a cross-section of an entire fiber, and it can be seen that the radial distribution of these inclusions is non-uniform, with their density being highest in the center of a fiber and reducing towards the periphery. EDX elemental analysis (performed in a line scan mode, with line crossing one of the inclusions as denoted in the Fig. 4a) indicates that in comparison to the bulk of SiC grains, these dark region are enriched in C and

depleted of Si (Fig. 4d), which means that they are likely to be precipitates of excess carbon.

Obtaining crystallographic information using EBSD was difficult, due to the relatively poor quality of the observed patterns. It was sufficient for pattern quality mapping, as presented in Fig. 3b, but not for the actual indexing and orientation mapping. This was overcome by the use of TKD. This technique uses electron-transparent samples, which can be used for TEM as well (as was done in the present work), with detected Kikuchi patterns produced by the electrons that were transmitted through the sample. Due to the reduction of interaction volume, the lateral resolution significantly increases. It can be further improved by the use of recently developed on-axis configuration (on-axis TKD), where the scintillator is located directly beneath the sample in TEM-like geometry [39].

Crystallographic indexing with TKD confirmed that both matrix and fiber consist predominantly of cubic β -SiC.

A sample containing the arrangement of fibers similar to the one presented in Fig. 3a is not optimal for the determination of crystallographic texture. Since grains in the matrix are positioned radially, the growth direction of most of them doesn't coincide with any one reference direction. For texture analysis samples of a different kind were used: these were lifted out of the vicinity of a fiber that is approximately normal to the surface. This way, the plane of the sample contains parallel matrix grains all aligned in the direction of growth. Fig. 5a presents an example of a STEM image of one such sample, containing both fiber and matrix materials. Grain growth direction here is denoted by the horizontal arrow, which is in turn aligned to a horizontal X-axis during TKD mapping. The insert in Fig. 5 presents the corresponding TKD orientation map, displayed in IPFX coloring (inverse pole figure showing a horizontal

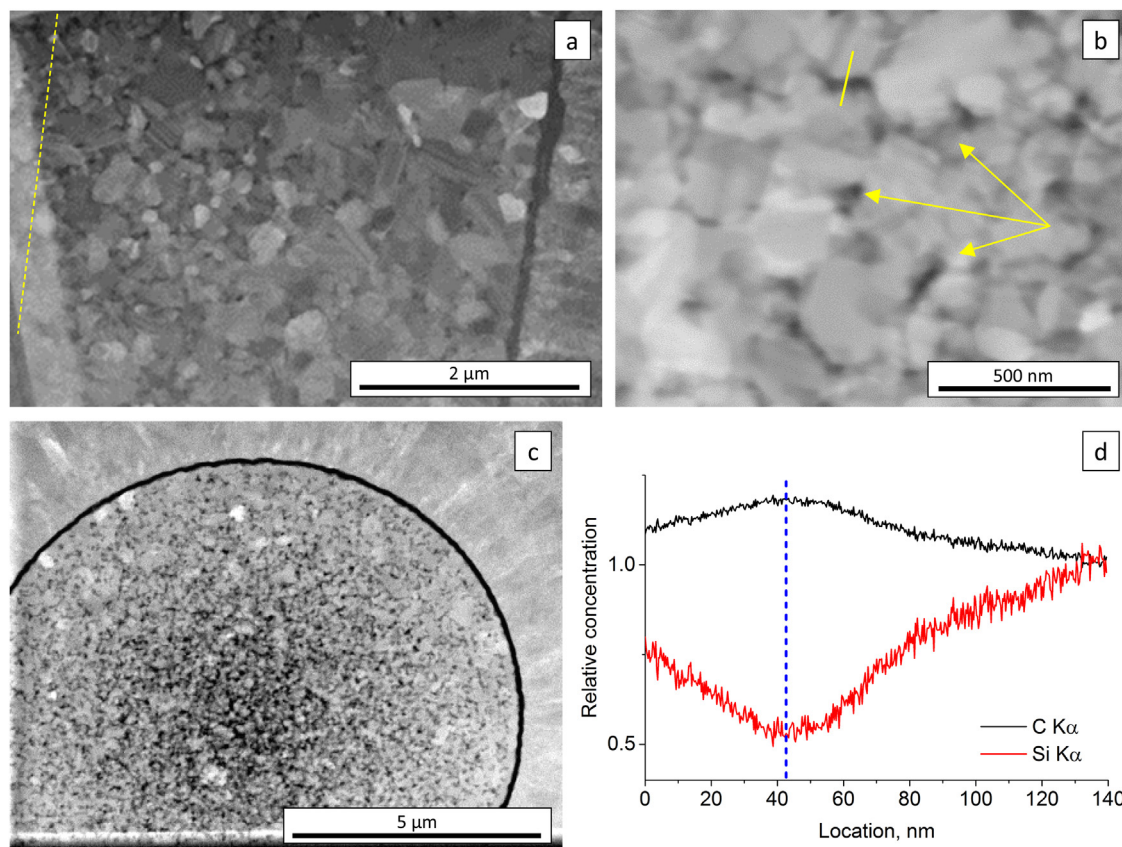


Fig. 4. TEM images: (a) cross-section of a fiber, dashed line corresponds to its central axis; (b) fiber material with the location of EDX line scan denoted by a line, arrows indicate inclusions at the grain boundaries; (c) radial distribution of the inclusions within a fiber; (d) EDX linescan – signals of C and Si.

direction), that is, map is color-coded in the reference direction which is aligned with the matrix grain growth direction.

Orientation map of this kind allows determination of the crystallographic texture, defined separately for matrix and fiber. The corresponding pole figures for matrix and fiber regions are presented in Fig. 5b and c. A significant difference in texture between matrix and fiber materials is evident. Matrix is noticeably textured in the growth direction (horizontal here), with preferred orientation being $\langle 111 \rangle$, with no texture in the other directions. This is in agreement with previously reported observations for the preferred growth direction in CVD grown SiC [40]. Meanwhile, there is no discernible texture in the fiber material.

TKD orientation map reveals microstructural features of a different kind, not easily resolvable by the direct TEM imaging. Fig. 6 shows the close-up of a specific region of the map that contains areas of different crystallographic orientation, as indicated by differing colours in IPFX map. The insert shows a misorientation profile measured along the line in the map (misorientation here is relative to the point of the origin of this line). It is evident that high-angle grain boundaries with 60° misorientation are present between the dissimilar regions; in addition they also have a common $\{111\}$ plane, and can therefore be identified as coherent $\Sigma 3$ twin boundaries, which are abundant in SiC [41].

3.2. Nanoindentation

For general characterization of the large-scale differences in mechanical properties between matrix and fiber materials nanoindentation was used. This was done in the form of line scans. Here indents of 300 nm depth were placed along the line with 1.5 μm

spacing between them. Fig. 7a shows an example of a line scan used, running both through matrix and fiber. Nanoindentation measurements were performed in CSM mode, where hardness and elastic modulus are recorded as a function of depth, as shown in Fig. 7b.

It should be noted that with indents located so close to each other it is conceivable that they might influence the results of measurements from each other. In order to clarify whether this is taking place, two rectangular 4 by 4 indent arrays were placed in the matrix, with different spacings between them – 1.5 μm in one case (i.e. same as in the line scans) and 15 μm in another, which served as a reference. No difference in the averaged measured values of hardness and modulus from each indent was observed. This indicates that plastic zone is extremely confined, and that the values of hardness measured in the described manner are indeed representative of the material's properties.

Fig. 8 shows the coordinate dependence of the hardness and modulus in the vicinity of a fiber, averaged over multiple line scans in the depth range 120–280 nm were averaged, where surface effects due to roughness are minimized (see Fig. 7b). Error bars here and in all subsequent graphs represent the standard deviation of measured values. It is evident that there is a significant difference between matrix and fiber materials. Hardness and modulus of fibers tend to be significantly lower than those of matrix. Hardness of the matrix is ~ 40 GPa, modulus is ~ 460 GPa. In addition, a fiber itself is very non-uniform, with values changing from those close to the ones of matrix at the periphery, to much lower near the center of the fiber, i.e. ~ 19 GPa hardness, ~ 260 GPa modulus.

This difference in mechanical properties can be explained by the presence of C residue at the grain boundaries, as observed in

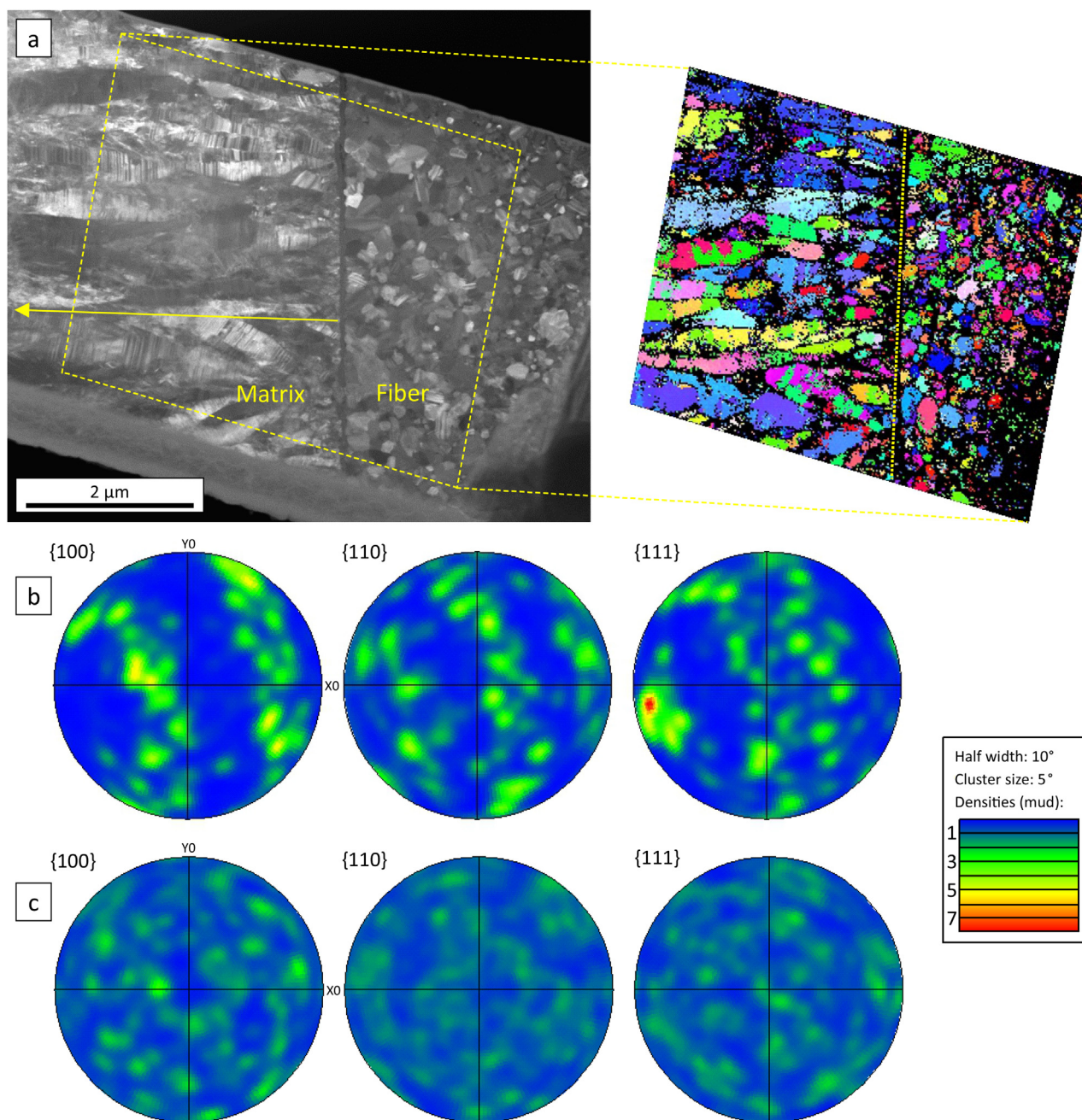


Fig. 5. (a) TEM image of the microstructure and the corresponding IPFX map. The arrow represents the direction of the grain growth. The vertical dashed line in the IPFX map represents the location of the interlayer; (b) pole figures of the matrix; (c) pole figures of the fiber.

STEM images. Indeed the amount of C within the grain is variable – it is highest around the center of the fiber and decreases outwards; at the very periphery of the fiber it is essentially absent, in agreement with the results presented in Ref. [25]. This correlates well with the observed dependences of hardness and modulus – the higher is excess C content, the lower they are; at the fiber periphery, where the amount of C is low and so material is close to pure near-stoichiometric SiC – like matrix – the values are close to that of the matrix. Reduced hardness and modulus of a material as a whole is therefore due to the lower hardness and modulus of this residual C.

Measured values of elastic modulus can be compared to the literature data of the macroscopic testing. Measurements in the

matrix are best compared to the measurements on polycrystalline CVD (chemical vapour deposition) SiC. Nanoindentation yields a value of ~460 GPa, while the values found in the literature range between ~415 and ~460 GPa [42–44]. On the other hand, given the non-uniformity of the fiber properties, in order to compare them to the results of tensile tests of the whole Tyranno SA fibers the values of modulus should be averaged over the cross-section of the fiber; averaged modulus is ~365 GPa, with literature values being 375–380 GPa [45,46]. Thus values of elastic modulus obtained by nanoindentation are in good agreement with those obtained by other means, such as tensile testing or impulse-excitation technique, in macroscopic samples. This is important for the ability to develop a microstructurally-informed model of composite's

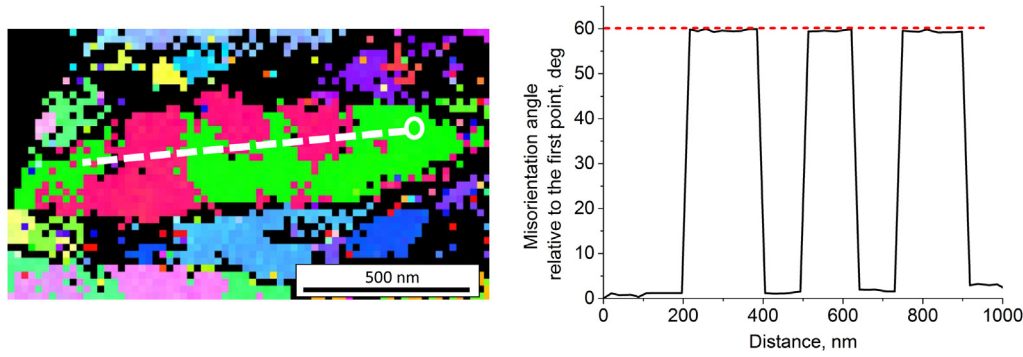


Fig. 6. Close-up of a series of twin boundaries and a misorientation profile along the denoted line, relative to the first point (indicated by a circle); dashed line denotes misorientation of 60°.

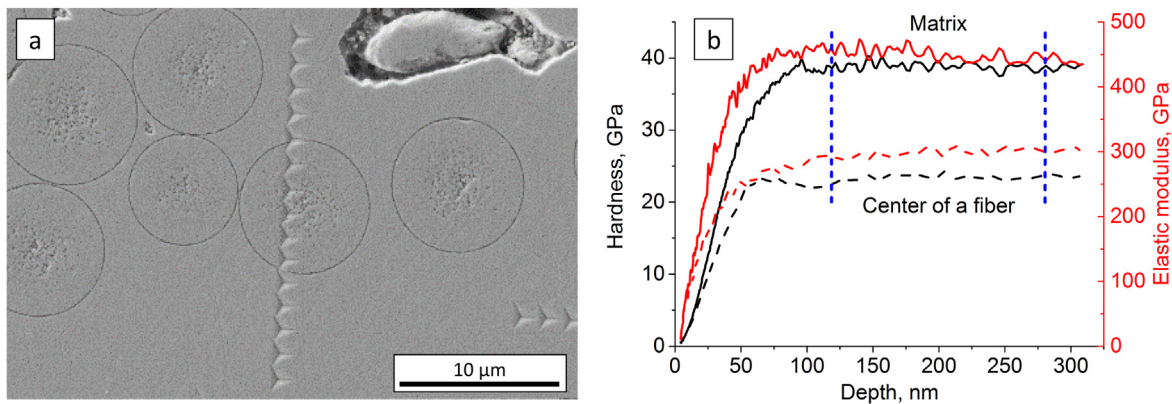


Fig. 7. (a) Example of a line of indents, crossing a matrix region and one of the fibers; (b) typical depth dependence of hardness (filled symbols) and modulus (hollow symbols) as a function of depth for the indents placed within the matrix (solid lines) and close to the center of a fiber (dashed lines); vertical lines denote the depth range used for averaging.

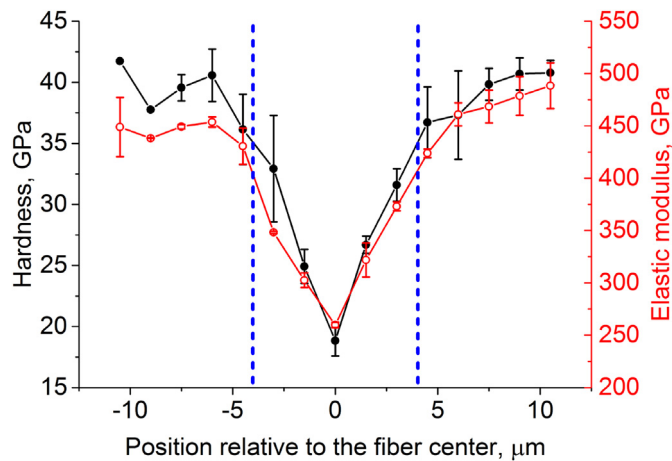


Fig. 8. Hardness (filled symbols) and modulus (hollow symbols) as a function of distance from the fiber center, averaged over multiple line scans crossing the fibers; vertical dashed lines denote the typical dimensions of a fiber.

behaviour, since representative data can be obtained from a very small volume of material. Producing composite samples by CVI is a lengthy process, duration of which scales with the amount of material produced; thus, minimization of this amount ensures much faster development cycle, where multiple different composite designs (e.g., with different CVI growth conditions, interfacial structures etc) can be manufactured and investigated quickly.

3.3. Microcantilever testing

In order to test the fracture behaviour of different constituents of the composite, microcantilevers were placed at various characteristic locations – the interphases, matrix and fibers. It should be noted that, since properties of the fibers are radially non-uniform (as revealed by nanoindentation measurements), cantilevers within them are oriented axially (as shown in Fig. 1b) and placed as close as possible to the axis of the fiber. This way, they do not cross regions of different properties within a fiber (and only contain fiber material), so that non-uniformity of properties along a cantilever is eliminated. On the other hand, the non-uniformity across the cantilever is inevitable since microstructure and chemical composition of a fiber are inherently non-uniform (Figs. 4c and 8). Having cantilevers at the axis of a fiber ensures that the region which is most different from the matrix (Fig. 8) is probed. Despite the cross-sectional non-uniformity, since all tested cantilevers were similar both in volume and in their location within a fiber, the results obtained from them are still comparable. This should also allow for easy future comparisons between different fibre types in use across the nuclear and aerospace industries.

Stress-strain curves were obtained from the measured load-displacement curves using equations derived from the simple beam theory, as in Ref. [47]:

$$\sigma = \frac{24PL}{wh^2} \quad (1)$$

$$\varepsilon = \frac{2h\delta}{L^2} \quad (2)$$

Here P is load, δ is displacement, L – length of a tested part of a cantilever (i.e. the distance between the cantilever's base and position of a loading indent), w – width of a cantilever and h – its height.

During the microstructural study it has been established that the matrix consists of elongated grains, with multiple types of boundaries within it (i.e. twin boundaries, grain boundaries, boundaries between nested rings and between domains of matrix originating from different fibers). It is conceivable that fracture behaviour of the matrix material can be different, depending on how crack propagates relative to the local direction of the grains. In order to investigate this, cantilevers in the matrix were placed at the specific orientations with respect to the grains in the matrix, namely, in longitudinal direction (with axis of a cantilever being parallel to the grains) and transverse direction (with axis of cantilever being normal to the grains).

Fig. 9 shows the results of the fracture tests performed on cantilevers in different constituents of the composite. Data points presented are averaged values over several tests (6 for interphase, 7 for fiber, 5 for transverse and 6 for longitudinal orientations in the matrix), with error bars corresponding to their standard deviations. It is evident that they demonstrate very different fracture properties. Interphases are the weakest points, with lowest fracture stress, ~2.6 GPa, and strain at fracture, ~3%. Material of the fibers is somewhat stronger, fracturing at ~6.4 GPa and ~6.5% strain, and matrix material is the strongest, ~21.5 GPa and ~12%, and there is no systematic difference between the longitudinal and transverse cantilevers.

Fracture toughness was calculated using the equation for stress intensity factor for straight notches determined using finite element compliance analysis (from Ref. [33]):

$$K = \frac{12PL_n}{wh^2} * 1.12\sqrt{\pi\alpha} * \left(1 + 0.123\alpha' + 5.456\alpha'^2 + 0.073\alpha'^3 - 0.023\alpha'^4\right) \quad (3)$$

Here P is the load, L_n the distance from the notch to the load point, w and h are respectively the cross-sectional width and height of a cantilever, α the depth of a notch and α' defined as α/h . This

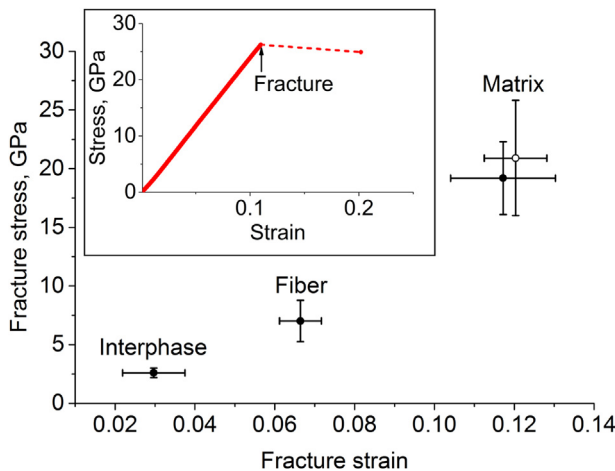


Fig. 9. Results of the fracture tests from cantilevers in different components of the composite; two values for the matrix are from the longitudinal (hollow symbol) and transverse (filled symbol) cantilevers. Insert – a stress-strain curve of a typical test.

equation is valid $\alpha' < 0.4$, as was indeed the case for the tested cantilevers. Fig. 10 presents the values of fracture toughness obtained in such a way for the cantilevers placed on different components of the composite. Number of tests performed was 4 for interphase, 5 for fiber, 3 and 2 respectively for the transverse and longitudinal directions in the matrix. Similarly to fracture stress, the comparison demonstrates that toughness is highest in the matrix (~4.25 $\text{MPa}\cdot\text{m}^{1/2}$), again without a systematic difference between cantilevers at different orientations relative to the direction of grain growth, lowest at the interphase (~0.8 $\text{MPa}\cdot\text{m}^{1/2}$), with fibers being intermediate (~2 $\text{MPa}\cdot\text{m}^{1/2}$).

Published data are available on fracture toughness of monolithic (non-composite) SiC ([48–51]). They show large scatter, with the reported values, derived from various macroscopic testing techniques, ranging from ~2.3 to ~5.1 $\text{MPa}\cdot\text{m}^{1/2}$. Literature data on Tyranno SA fibers give a value of fracture toughness of $2.7 \pm 0.4 \text{ MPa}\cdot\text{m}^{1/2}$, measured in notch tensile tests [52]. Thus the values of K_{IC} obtained for matrix (being the most comparable to monolithic material) and fibers are in reasonable agreement with the bulk data from literature sources. On the other hand, fracture toughness of the interphases cannot be measured using the bulk testing, despite this being the key parameter in failure of the composites.

Typical fracture surfaces of cantilevers in different components are presented in Fig. 11. Fig. 11a presents a fractured cantilever at the interphase, with the visible surface being a surface of that fiber. On the other hand, Fig. 11b shows a cantilever within a fiber, so that visible fracture surface shows the internal structure. Note the presence of dark C inclusions in Fig. 11b, corresponding to near-central region of a fiber, and their absence in Fig. 11a, which shows the outermost region of a fiber, in accordance to the radial distribution of residual C, as presented in Fig. 4. Of note is a significant difference in fracture surfaces between longitudinal and transverse (relative to the grain growth direction) cantilevers in the matrix (Fig. 11c and d). Transverse cantilevers' fracture surfaces feature the elongated grains running across the fracture surface. In contrast to this, the longitudinal cantilevers contain such grains face-on. Thus, the corresponding fracture surface doesn't show elongated features, but rather more equiaxed instead. These features are cross-sections of the elongated grains – which are long but rather narrow. This becomes more evident in the STEM images presented below.

In order to rationalize the observed fracture behaviour and the crack propagation the lift-out TEM samples were manufactured out of tested cantilevers. This was technically challenging, because

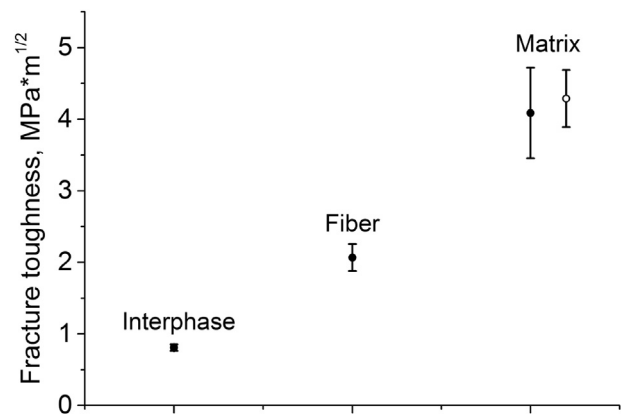


Fig. 10. Fracture toughness of different components of a composite. Two values for the matrix are from the longitudinal (hollow symbol) and transverse (filled symbol) cantilevers.

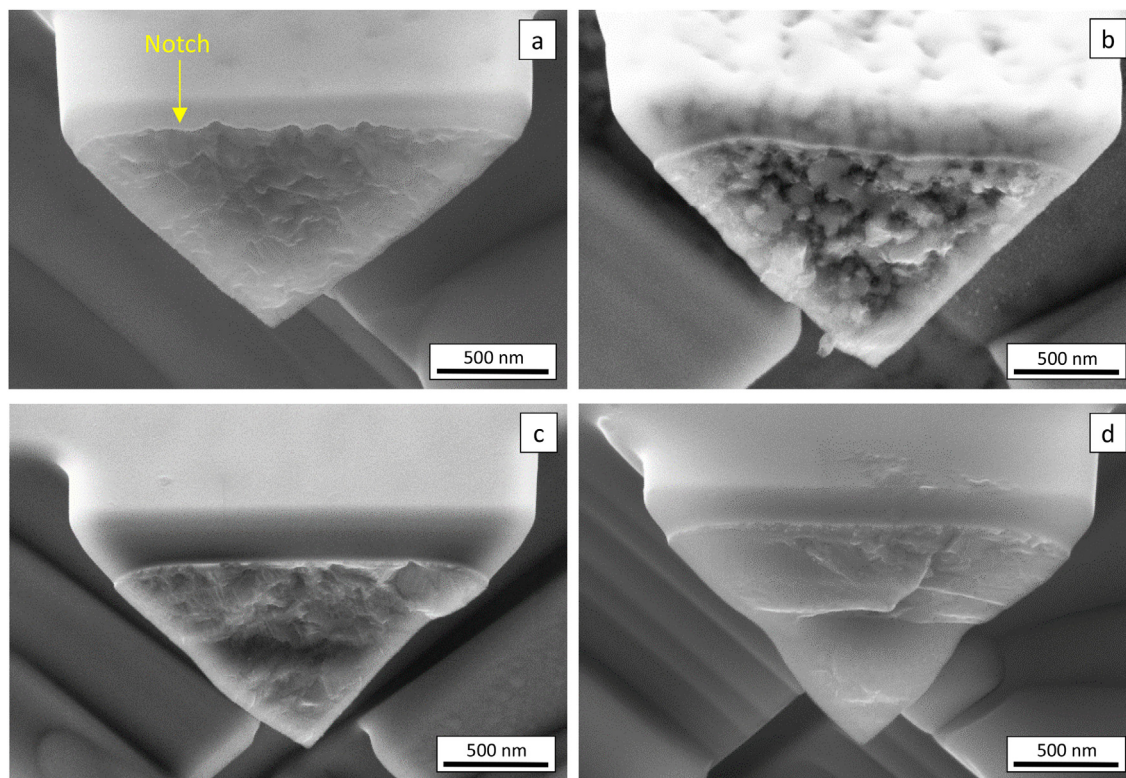


Fig. 11. Typical fracture surfaces of the notched cantilevers in different constituents: (a) interphase (remaining base of the cantilever, visible in the image, is in the fiber); (b) fiber; (c) matrix – longitudinal direction; (d) matrix – transverse direction. Note the geometry of the visible straight notch.

during a typical fracture test, the cantilever being tested is completely broken off when fracture occurs; this makes it difficult to observe the exact relation between the location of the crack and the grain boundaries or other microstructural features which might influence its propagation. Therefore it is necessary to ensure that the fracture has been initiated but at the same time the crack has not propagated through the whole thickness of a cantilever so that the beam is attached to its base by a narrow ligament. In order to achieve this, the test must be constantly monitored and manually stopped as soon as load drop occurs in the load-displacement curve, indicating that fracture has been initiated. In case of cantilevers placed within a bulk matrix or a fiber this is difficult to accomplish because once fracture is initiated, the crack propagates fast and it is hard to react and stop the load. In order to circumvent this obstacle, cantilevers with the chevron notch were implemented [53]. In this geometry, the quadrangular chevron is introduced into the beam. This way, the stress concentration is introduced where the fracture starts; increasing width of the material ligament through which crack is propagating ensures that it propagates in a slower stable manner. Using cantilevers with chevron notches it is possible to stop the loading such that the cantilever is not broken off and can be therefore lifted out for manufacturing of a TEM sample. For cantilevers at the interphases use of a chevron notch is not necessary since there fracture occurs more slowly and so testing can be stopped without complete fracture.

Once partial fracture has been achieved, the entire cantilever is first embedded in a protective Pt layer so that the small remaining ligament is not broken during the lift-out; then it is lifted out of the surface, and the area surrounding the location of the crack is thinned down to electron transparency.

Fig. 12 presents the TEM images of the fractured cantilevers.

Fig. 12a shows the propagation of fracture at the fiber-matrix interphase. Area to the left of the crack in the image is matrix, area to the right is fiber, the dark stripe in between is PyC interlayer. Certain amount of Pt deposited on the top surface of the cantilever to form a protective layer penetrated into the crack, forming the brighter stripes along the crack walls. It is evident that the crack propagation is confined to the interphase region, without straying into bulk material, neither matrix nor fiber. The insert in the Fig. 12a shows an EDX elemental map of the highlighted region. It confirms that crack predominantly runs along the boundary between the C interlayer and the SiC fiber, although it seems to have initiated within the volume of the interlayer. Fig. 12b shows the propagation of fracture within the notched cantilever located entirely within the fiber. It appears that fracture has both intergranular and transgranular features. In the location X it is following the boundary of a large grain. In the location Y, however, the crack is cutting through the grain's volume. Fig. 12c shows the propagation of fracture within the notched cantilever in the bulk matrix and oriented in the transverse direction, i.e. elongated grains in the matrix are normal to the axis of a cantilever. Here it can be seen clearly that fracture is transgranular, with crack not being associated with any of the present grain boundaries. Fig. 12d shows the propagation of fracture within the notched cantilever located entirely within the matrix and oriented in the transverse direction, i.e. elongated grains in the matrix are parallel to the axis of a cantilever. Similarly to the cantilever oriented transversely, here the fracture is transgranular.

The observed differences in crack propagation can be correlated with the results of fracture tests. The difference between the fiber and the matrix materials can be traced back to C precipitates. It can be seen that the cracks in the fibers are, at least at some instances, associated with the grain boundaries, where C is present, although

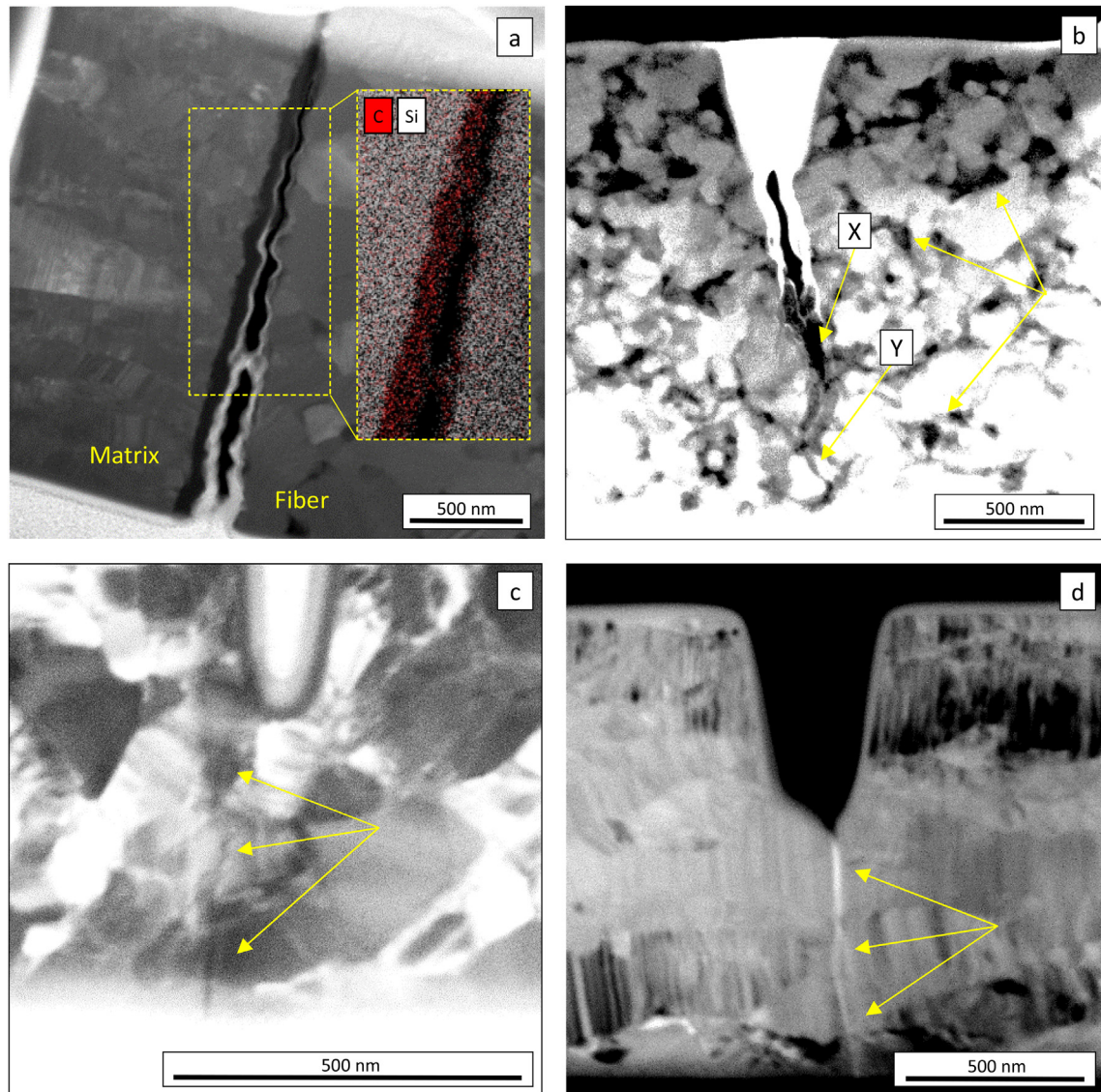


Fig. 12. TEM images of the fractured cantilevers: (a) at the matrix-fiber interphase; insert – EDX elemental map of the highlighted area; (b) in the bulk fiber, arrows denote the C precipitates at grain boundaries, X denotes the instance of intergranular crack propagation, Y the instance of transgranular crack propagation; (c) in the bulk matrix, transverse orientation; here and in (d) the arrows are to guide the eye along the crack; (d) located in the bulk matrix, longitudinal orientation. Cantilever in (a) is unnotched, all the others are notched.

this does not necessarily have to be the case – transgranular crack propagation has also been observed. On the other hand, within the matrix, where these precipitates are absent, fracture is exclusively transgranular. The fact that in the presence of carbon intergranular fracture is preferable implies that it makes grain boundaries weaker, which can be suggested as a reason for lower fracture toughness, as is indeed observed in cantilever tests.

Another correlation can be drawn between the results of tests performed at different orientations of cantilevers relative to the orientation of grains within the matrix. The primary fracture mechanism is transgranular regardless of how cantilevers are oriented. This should result in similar fracture properties, and indeed no systematic difference in fracture toughness can be seen in the cantilever tests. This suggests that various kind of microstructural features in Fig. 3 are in fact of no particular influence of the fracture behaviour of the matrix. The primary result of the existence of the complicated microstructure within the matrix is the introduction of large number of grain boundaries. But since fracture appears to be

primarily transgranular and not dominated by grain boundaries, it can be surmised that this is inconsequential and that for the purposes of modelling matrix can be treated as a uniform and isotropic medium with respect to fracture – but not homogeneous, since it contains porosity, including small submicron-sized pores. On the other hand, for the fibers the assumption of uniformity is not correct, as there the presence of carbon at the grain boundaries might have an impact on fracture behaviour, and distribution of carbon is non-uniform. The amount of grain boundary C is high in the center and lower or almost negligible at the periphery, and thus fracture properties should be considered as having radial distribution within the fiber (similarly to how hardness is radially non-uniform).

In addition it should also be noted that the values of both fracture stress/strain and fracture toughness of the matrix material exhibit significantly larger scatter compared to those of fibers and interphases (Figs. 9 and 10). It is likely related to the presence of submicron-sized porosity in the matrix, as revealed by TEM

analysis. It is difficult to determine the exact internal structure of each individual cantilever; however, it is likely that cantilevers without pores are more resistant to crack initiation as well as more resistant to crack propagation than those without.

4. Conclusions

Micromechanical assessment of the individual components of the SiC fiber reinforced SiC matrix composite grown by CVI method – fiber and matrix materials, and interphases – has been performed. Its results were rationalized using the microstructural characterisation of the corresponding components. Main findings can be summarized as follows:

The microstructures of the constituents of the composite have been investigated using SEM, STEM, EBSD and TKD. It has been observed that fiber contains equiaxed grains with the carbon precipitates at the grain boundaries, in accordance to earlier published findings. Distribution of this precipitates is non-uniform: their density is higher in the center of the fibers and decreases radially outwards, with periphery being almost carbon-free; distribution of the grain size is non-uniform as well, with grain size increasing outwards.

The microstructure of the matrix is complex, with the grains organized into several levels. Each fiber is surrounded by a system of elongated grains, due to the material being deposited from the vapour phase during the growth process. Preferred growth direction was determined to be $\langle 111 \rangle$. These grains often feature twinning. They form a series of concentric rings, which appear due to the discontinuities in during the growth. Finally, grains originating at each fiber form a domain of matrix material; domain boundaries often feature submicron-sized porosity associated with the mismatched grains belonging to different domains.

Nanoindentation revealed the significant difference in hardness between the fiber and the matrix material, and at the same time a strong radial non-uniformity of hardness within a fiber itself. Hardness changes from ~ 40 GPa in the matrix to ~ 17 GPa in the center of the fiber, with intermediate radial locations in the fiber having intermediate values; similarly elastic modulus changes from ~ 460 GPa to ~ 260 GPa. This correlates with the distributions of excess carbon decorating the grain boundaries, and the presence of this carbon can be suggested as a reason for the difference.

Fracture tests were performed using the microcantilevers, both unnotched and straight-notched. Size of the used cantilevers was sufficiently small to enable placing them within individual composite constituents – matrix and fiber, as well as, crucially, interphases. Following these tests, TEM imaging of the fractured cantilevers was used to study the crack paths in different composite constituents. It was determined that at the interphase cracks tend to follow the fiber-interlayer boundary, which is a weak point where fracture occurs at the lowest stress 2.3 GPa, with toughness being $\sim 0.8 \text{ MPa}\cdot\text{m}^{1/2}$. Fracture within the matrix is transgranular regardless of how a cantilever is oriented relative to the direction of grain growth, which agrees with the observation that there seems to be no systematic difference between fracture stress (~ 21 GPa) and fracture toughness ($\sim 4.25 \text{ MPa}\cdot\text{m}^{1/2}$) measured by cantilevers with different orientations. Finally, in the fibers the fracture occurs both within grains and along the grain boundaries decorated by carbon precipitates. The weakening of the grain boundaries by these precipitates explains the reduced fracture stress (~ 8 GPa) and toughness ($\sim 2 \text{ MPa}\cdot\text{m}^{1/2}$) of the fibers compared to the matrix.

Measured values of the properties that can be directly compared to those obtained independently in macroscopic tests – elastic modulus and fracture toughness – are in agreement with the results of those measurements. This supports the validity of the micromechanical approach to investigation of localized mechanical

properties of the constituents of SiC composites in-situ within the composite structure. On the other hand, fracture toughness of the interphases cannot be probed without the use of micromechanical tools; and for SiC-SiC composite it was directly measured for the first time.

These results demonstrate the possibility of the in-situ evaluation, using the methodology described here, of modification and/or degradation of constituent properties during simulated degradation, which could be irradiation damage in nuclear grade materials or hot oxidation in aerospace materials, which can then be correlated with processing variables. This ability to obtain representative data from small volumes of material will further reduce the time and cost of ceramic composite development.

More specifically, these results suggest the important directions for the development of accurate yet computationally tractable models to understand the properties of the SiC-SiC composite components. The matrix can be treated as an isotropic medium, its microstructure disregarded and only distribution of porosity being relevant. Within the fibers a radial distribution of mechanical properties should be assumed (as was directly observed in case of hardness and surmised regarding fracture) due to the radially non-uniform distribution of carbon precipitates at the grain boundaries. The fracture toughness of the interface in SiC-SiC composite is now known, and this is a key parameter in crack propagation in this region.

Acknowledgements

This work has been carried out through the EPSRC funded grant EP/N017110/1. D. Armstrong acknowledges support from the Royal Academy of Engineering in the form of a Research Fellowship. This work was also supported by the U.S. Department of Energy (DOE), Office of Nuclear Energy's Nuclear Science User Facilities (NSUF) program and the DOE-NEUP program 15-8439. Presented data are available online at Oxford University Research Archive, <https://doi.org/10.5287/bodleian:xQwyPompm>.

References

- [1] C.H. Carter Jr., R.F. Davis, J. Bentley, Kinetics and mechanisms of high-temperature creep in silicon carbide: II, chemically vapor deposited, *J. Am. Ceram. Soc.* 67 (1984) 732–740.
- [2] E.A. Gulbransen, S.A. Jansson, The high-temperature oxidation, reduction, and volatilization reactions of silicon and silicon carbide, *Oxid. Metals* 4 (1972) 181–201.
- [3] H. Kikuchi, R.K. Kalia, A. Nakano, P. Vashishta, P.S. Branicio, F. Shimojo, Brittle dynamic fracture of crystalline cubic silicon carbide (3C-SiC) via molecular dynamics simulation, *J. Appl. Phys.* 98 (2005) 103524.
- [4] S. Yajima, J. Hayashi, Development of a silicon carbide fibre with high tensile strength, *Nature* 261 (1976) 683–685.
- [5] J.A. DiCarlo, in: N.P. Bansal, J. Lamon (Eds.), *Advances in SiC/SiC Composites for Aero-Propulsion in Ceramic Matrix Composites: Materials, Modelling and Technology*, John Wiley & Sons, 2015.
- [6] G. Gardiner, *Aeroengine Composites, Part I: the CMC Invasion*, 2015. Composites World.
- [7] M. Fellet, Ceramic-matrix composites take the heat, *MRS Bull.* 40 (2015).
- [8] F.W. Zok, Ceramic-matrix composites enable revolutionary gains in turbine engine efficiency, *Am. Ceram. Soc. Bull.* 95 (2016).
- [9] R.J. Price, Properties of silicon carbide for nuclear fuel particle coatings, *Nucl. Technol.* 35 (1977) 320–336.
- [10] K.A. Terrani, Y. Yang, Y.-J. Kim, R. Rebak, H.M. Meyer III, T.J. Gerczak, Hydrothermal corrosion of SiC in LWR coolant environments in the absence of irradiation, *J. Nucl. Mater.* 465 (2015) 488–498.
- [11] S.J. Zinkle, K.A. Terrani, J.C. Gehin, L.J. Ott, L.L. Snead, Accident tolerant fuels for LWRs: a perspective, *J. Nucl. Mater.* 448 (2014) 374–379.
- [12] K. Yueh, D. Carpenter, H. Feinroth, Clad in clay, *Nucl. Eng. Int.* 55 (2010) 75–87.
- [13] X. Zhou, S. Zhao, P. Mummery, J. Marrow, Studying SiC/SiC composites by X-ray tomography, *Key Eng. Mater.* 602–603 (2014) 416–421.
- [14] W.B. Hillig, Melt infiltration approach to ceramic matrix composites, *J. Am. Ceram. Soc.* 71 (1988) 96–99.
- [15] L.V. Interrante, C.W. Whitmarsh, W. Sherwood, Fabrication of SiC matrix composites using a liquid polycarbosilane as the matrix source, *Ceram. Trans.*

- 58 (1995) 111–118.
- [16] Y. Katoh, S.M. Dong, A. Kohyama, Thermo-mechanical properties and microstructure of silicon carbide composites fabricated by nano-infiltrated transient eutectoid process, *Fusion Eng. Des.* 61–2 (2002) 723–731.
- [17] F.H. Gern, Liquid silicon infiltration: description of infiltration dynamics and silicon carbide formation, *Composites Part A* 28A (1997) 355–364.
- [18] R. Naslain, J.Y. Rossignol, P. Hagenmuller, F. Christin, L. Heraud, J.J. Choury, Synthesis and properties of new composite materials for high temperature applications based on carbon fibers and C-SiC and C-TiC hybrid matrices, *Rev. Chim. Miner.* 18 (1981) 544–564.
- [19] M.E. Sawan, N.M. Ghoniem, L. Snead, Y. Katoh, Damage production and accumulation in SiC structures in inertial and magnetic fusion systems, *J. Nucl. Mater.* 417 (2011) 445–450.
- [20] C.P. Deck, H.E. Khalifa, B. Sammulu, T. Hilsabeck, C.A. Back, Fabrication of SiC–SiC composites for fuel cladding in advanced reactor designs, *Prog. Nucl. Energy* 57 (2012) 38–45.
- [21] L.L. Snead, T. Nozawa, Y. Katoh, T.S. Byun, S. Kondo, D.A. Petti, Handbook of SiC properties for fuel performance modelling, *J. Nucl. Mater.* 371 (2007) 329–377.
- [22] R.J. Kerans, R.S. Hay, T.A. Parthasarathy, M.K. Cinibulk, Interface design for oxidation-resistant ceramic composites, *J. Am. Ceram. Soc.* 85 (2002) 2599–2632.
- [23] X.W. Yin, L.F. Cheng, L.T. Zhang, N. Travitzky, P. Greil, Fibre-reinforced multifunctional SiC matrix composite materials, *Int. Mater. Rev.* 62 (2017) 117–172.
- [24] D. Hull, T.W. Clyne, *An Introduction to Composite Materials*, second ed., Cambridge University Press, 1996.
- [25] D. Frazer, M.D. Abad, D. Krumwiede, C.A. Back, H.E. Khalifa, C.P. Deck, P. Hosemann, Localized mechanical property assessment of SiC/SiC composite materials, *Composite A* 70 (2015) 93–101.
- [26] https://www.ube.com/contents/en/chemical/continuous_inorganic_fiber/tyranno_fiber.html.
- [27] C. Sauder, J. Lamon, Tensile creep behavior of SiC-based fibers with a low oxygen content, *J. Am. Ceram. Soc.* 90 (2007) 1146–1156.
- [28] M.W. Phaneuf, J. Li, T. Malis, High resolution FIB as a general materials science tool, *Microsc. Microanal.* 4 (1998) 492–493.
- [29] J.R. Michael, P.G. Kotula, Low energy Ga⁺ and Ar⁺ ion milling for improved EBSD sample preparation, *Microsc. Microanal.* 14 (Supplement 2) (2008).
- [30] W.C. Oliver, G.M. Pharr, An improved technique for determining hardness and elastic modulus using load and displacement sensing indentation experiments, *J. Mater. Res.* 7 (1992) 1564.
- [31] D. Di Maio, S.G. Roberts, Measuring fracture toughness of coatings using focused-ion-beam-machined microbeams, *J. Mater. Res.* 20 (2005) 299–302.
- [32] D.E.J. Armstrong, A.J. Wilkinson, S.G. Roberts, Measuring anisotropy in Young's modulus of copper using microcantilever testing, *J. Mater. Res.* 24 (2009) 3268.
- [33] A.D. Norton, S. Falco, N. Young, J. Severs, R.I. Todd, Microcantilever investigation of fracture toughness and subcritical crack growth on the scale of the microstructure in Al₂O₃, *J. Eur. Ceram. Soc.* 35 (2015) 4521–4533.
- [34] OIM Data Collection Manual, EDAX, 2013.
- [35] S.I. Wright, M.M. Nowell, EBSD image quality mapping, *Microsc. Microanal.* 12 (2006) 72–84.
- [36] S. Schamm, A. Mazel, D. Dornig, J. Sève, HREM identification of "one-dimensionally-disordered" polytypes in the SiC (CVI) matrix of SiC/SiC composites, *Microsc. Microanal. Microst.* 2 (1991) 59–73.
- [37] G. Wei, W. Qin, G. Wang, J. Sun, J. Lin, R. Kim, D. Zhang, K. Zheng, The synthesis and ultraviolet photoluminescence of 6H-SiC nanowires by microwave method, *J. Phys. Appl. Phys.* 41 (2008) 235102.
- [38] R. Dong, W. Yang, P. Wu, M. Hussain, Z. Xiu, G. Wu, P. Wang, Microstructure characterization of SiC nanowires as reinforcements in composites, *Mater. Char.* 103 (2015) 37–41.
- [39] E. Brodu, E. Bouzy, J.-J. Fundenberger, J. Guyon, A. Guittou, Y. Zhang, On-axis TKD for orientation mapping of nanocrystalline materials in SEM, *Mater. Char.* 130 (2017) 92–96.
- [40] R.R. Naslain, Ceramic matrix composites, *Phil. Trans. Roy. Soc. A* 351 (1995) 485–496.
- [41] D.J. Smith, N.W. Jepps, T.F. Page, Observations of silicon carbide by high resolution transmission electron microscopy, *J. Microsc.* 114 (1978) 1–18.
- [42] J.F. Shackelford, W. Alexander (Eds.), *Materials Science and Engineering Handbook*, CRC Press LLC, Boca Raton, 2001.
- [43] G.A. Graves, D. Iden, CVD Silicon Carbide Characterization, RL-TR-94-122 Final Technical Report, 1994.
- [44] K.M. Jackson, Fracture strength, elastic modulus and Poisson's ratio of polycrystalline 3C thin-film silicon carbide found by microsample tensile testing, *Sensor. Actuator.* 125 (2005) 34–40.
- [45] J.A. DiCarlo, H.-M. Yun, Non-oxide (Silicon Carbide) Fibers, *Handbook of Ceramic Composites* Springer, Boston, MA, 2006, pp. 99–115.
- [46] https://www.ube.com/contents/en/chemical/continuous_inorganic_fiber/tyranno_fiber.html.
- [47] D.E.J. Armstrong, *Measuring Elastic, Plastic and Fracture Properties Using Micro-cantilever Testing*, PhD thesis, 2009.
- [48] I. Merkel, U. Messerschmidt, Fracture toughness of sintered SiC ceramics: a comparison between different methods, *Mater. Sci. Eng., A* 151 (1992) 131–135.
- [49] S.G. Seshadri, M. Srinivasan, L. King, Indentation fracture testing of ceramics, *Ceram. Eng. Sci. Proc.* 4 (1983) 853–863.
- [50] H. Kodama, T. Miyoshi, Study of fracture behaviour of very fine-grained silicon carbide ceramics, *J. Am. Ceram. Soc.* 73 (1990) 3081.
- [51] K. Niihara, Mechanical properties of chemically vapor deposited nonoxide ceramics, *Am. Ceram. Soc. Bull.* 63 (1984) 1160–1164.
- [52] S. Ochiai, H. Okuda, T. Inshikawa, M. Sato, T. Inoue, Fracture toughness of crystalline silicon carbide fiber (Tyranno-SA3), *J. Am. Ceram. Soc.* 89 (2006) 2571–2576.
- [53] K. Matoy, H. Schönherr, T. Detzel, T. Schöberl, R. Pippin, C. Motz, G. Dehm, A comparative micro-cantilever study of the mechanical behavior of silicon based passivation films, *Thin Solid Films* 518 (2009) 247–256.